SAND2017-1376C

Resonance Dynamics in Compressible Cavity Flows using Time-Resolved Particle Image Velocimetry and Pressure Sensitive Paint

Justin L. Wagner,[1] Steven J. Beresh,[2] Katya M. Casper[3], Edward P. DeMauro,[4] Srinivasan Arunajatesan[5]
Sandia National Laboratories, Albuquerque, NM, 87185

The resonance modes in Mach 0.94 turbulent flow over a cavity having a length-to-depth ratio of five were explored using time-resolved particle image velocimetry and time-resolved pressure sensitive paint. Mode-switching occurred in the velocity field simultaneous with the pressure field. The first cavity mode corresponded to large-scale motions in shear layer and in the vicinity of the recirculation region, whereas the second and third modes contained organized structures associated with shear layer vortices. Modal surface pressures exhibited streamwise periodicity generated by the interference of downstream-traveling disturbances in shear layer with upstream-traveling acoustical waves. Because of this interference, the modal velocity fields also exhibited local maxima at locations containing pressure minima and vice-versa. Modal propagation velocities, based on cross-correlations of bandpass-filtered velocity fields, decreased with decreasing mode number as the modal activity resided in lower portions of the cavity. These propagation velocities also exhibited streamwise periodicity caused by wave interference. The measurements demonstrate that despite the complexities inherent in compressible cavity flows, many of the most prevalent resonance dynamics can be described with simple acoustical analogies.

I. Introduction

The flow over an open cavity generates large pressure fluctuations associated with broadband turbulence and cavity resonance [1], which can result in high levels of structural vibrations [2-5]. Since cavity flow is analogous in many ways to an open aircraft bay in flight, the subject has received much attention over the last sixty years as detailed in the review articles of Rockwell and Naudascher [6, 7], Rowley and Williams [8], and Cattafesta et al. [9]. In subsonic flows, when the cavity length-to-depth ratio L/D is less than about seven [10], an interaction of the cavity's acoustic field and free shear layer form a feedback loop that results in resonant oscillations [1]. The resonant modes are primarily longitudinal and in simple rectangular geometries, the tonal frequencies are reasonably predicted by the semi-empirical relation provided in the seminal work of Rossiter [1].

In comparison to modal frequencies, prediction of the modal amplitudes is much more difficult as the pressure magnitudes are sensitive functions of the flow conditions (boundary layer properties, Mach number, e.g.) as well as the cavity geometry (L/D and length-to-width ratio L/W, e.g.) [10]. Changes to geometric parameters such as L/W also lead to modifications of cavity turbulence levels and the shear layer growth rate [11 - 14], which in turn can alter the overall broadband fluid dynamic loading. Geometric complexities associated with real aircraft bays, such as inflow ramps and doors can also alter and enhance resonance tones [15] resulting in three-dimensional flow features [16, 17].

[1] Principal Member of the Technical Staff, Engineering Sciences Center, P.O. Box 5800, Mailstop 0825; jwagner@sandia.gov. AIAA Senior Member.
[2] Distinguished Member of the Technical Staff, Engineering Sciences Center, AIAA Associate Fellow.
[3] Senior Member of the Technical Staff, Engineering Sciences Center, AIAA Senior Member.
[4] Post-doctoral Appointee, Engineering Sciences Center, AIAA Member.
[5] Manager, Engineering Sciences Center, AIAA Senior Member.

This work is supported by Sandia National Laboratories and the United States Department of Energy. Sandia National Laboratories is a multi-program laboratory managed and operated by Sandia Corporation, a wholly owned subsidiary of Lockheed Martin Corporation, for the U.S. Department of Energy's National Nuclear Security Administration under contract DE-AC04-94AL85000

Other challenges lie in understanding the temporal behavior of resonating cavity flows. Cavity flow dynamics involve complex interactions of the mixing layer, recirculating flow, turbulence, and acoustic waves. Although a given cavity flow can be associated with several tonal frequencies, the tones do not necessarily occur simultaneously. Rather the dominant cavity mode can vary with time – a process known as 'mode-switching'. The idea for mode-switching was first proposed in the earlier works of Krishnamurty [18] and Sarohia [19], later proven in the experiments of Kegerise et al. [20, 21], and observed in the simulations of Larchevêque et al. [22] shortly thereafter. Fairly recently, direct numerical simulation (DNS) by Brès and Colonious [23] suggested that spanwise instabilities can lead to low-frequency modulations of Rossiter modes. An additional, unique view on cavity dynamics was given by Delprat [24] who theorized that cavity modes are not unique; rather they are modulations of a fundamental loop frequency. Despite these examples of recent progress, the dynamics of cavity flows, particularly in the high-speed regime, is an evolving research area. A common, quantitative consensus on the physical mechanisms of cavity tone modulations, and the relationship between resonance pressure fluctuations and cavity flow field dynamics in general, has yet to be achieved.

Experimental data capturing cavity flow field dynamics are required to develop and validate new theoretical models. Flow visualization methods show that large-scale coherent structures propagate in the shear layer of resonating, compressible cavity flows [1, 20, 21]. More quantitatively, in incompressible cavity flows, time-resolved particle image velocimetry (TR-PIV) and laser Doppler velocimetry (LDV) measurements have revealed periodic velocity variations associated with resonance [25 - 27] and have been used to quantify low-frequency, large-scale flapping motions in the shear layer [28]. In compressible flows, however, PIV measurements are typically made at repetition rates far too low to capture dynamics in a time-resolved fashion. To overcome this, researchers have pieced together spatial distributions using time-resolved point measurements of velocity and density [20, e.g.]. Stochastic estimation methods that create low-dimensional representations of the velocity field informed by time-resolved surface pressure data from sensors have also proved useful. For instance, Murray and Ukeiley [29] were able to successfully to track the effect of coherent flow structures on surface pressures at transonic Mach number. In another example, Murray et al. [30] used stochastic methods to suggest that Rossiter pressure fluctuations were primarily influenced by mean-shear velocity terms in Poisson's equation as opposed to non-linear, turbulent velocity fluctuation terms.

Here, PIV and surface pressure data are utilized to reveal new information on resonance flow field dynamics in compressible cavity flow. Recent advances in measurement technology have set the stage for high repetition rate measurements of cavity flow field dynamics using TR-PIV [32], as well as cavity surface pressures with time-resolved pressure sensitive paint (TR-PSP) [33, 34]. In the current work, both of these pacing measurement technologies, along with spectral analysis, are utilized to increase understanding of cavity resonance, particularly the relationship between surface pressure fluctuations and the dynamics in the flow field. Mode-switching, as measured in the pressure field, is first investigated in the velocity fields. The focus of the paper then shifts to the influence of the pressure field on the propagation and modulation of coherent structures in the velocity field.

II. Experimental Program

A. Trisonic Wind Tunnel (TWT)

Experiments were conducted in the blowdown-to-atmosphere TWT. The facility uses air as the test gas and has a test section enclosed in a pressurized plenum. Data were obtained at a freestream Mach number M_∞ of 0.94 (U_∞ = 311 m/s), which was determined using a freestream velocity measurement at the cavity entrance location and the assumption of isentropic expansion. Forty nine wind tunnel runs were made at this condition. Typical flow conditions for the experiments conducted in the 305 × 305 mm^2 test section are given in Table 1. The tunnel wall boundary layers developed naturally and were fully turbulent upon arrival at the test section. Previous measurements have indicated that the 99% wall boundary layer thickness at the cavity entrance is about 13 mm or about half the cavity depth.

Table 1: Typical TWT Experimental Conditions

M_∞	P_0, kPa	T_0, K	Re × 10^{-6}, /m
0.94	60	321	13

In subsonic cavity flows it is necessary to mitigate the undesirable acoustical interference associated with solid wind tunnel walls by placing an acoustic absorber in the wall opposite to the cavity [20, 35-36]. Described in a recent study by the current authors, the spanwise walls of subsonic test sections can also lead to acoustical

contamination if untreated [37]. To reduce these effects, the wall opposite the cavity and one spanwise wall were replaced with acoustic dampeners, which consisted of a porous wall, used typically for transonic testing, backed by acoustical absorption foam. The opposite spanwise wall was solid with a window providing a view for the PIV cameras.

B. Cavity

The cavity had a length L of 127 mm, width W of 127 mm, and depth D of 25.4 mm and was installed in the lower wall of the test section in experiments using PIV (Fig. 1a). In separate experiments using TR-PSP, the cavity was instead installed in the ceiling of the wind tunnel and the cavity floor was viewed through windows in the lower walls of the test section and plenum (Fig. 1b). With an L/D of 5, the cavity flow category is 'open' and expected to resonate [10]. The streamwise (x), wall-normal (y), spanwise (z) coordinate system originates at the spanwise center of the cavity leading edge. The wind tunnel floor is defined to be at $y = 0$, with positive y pointing away from cavity.

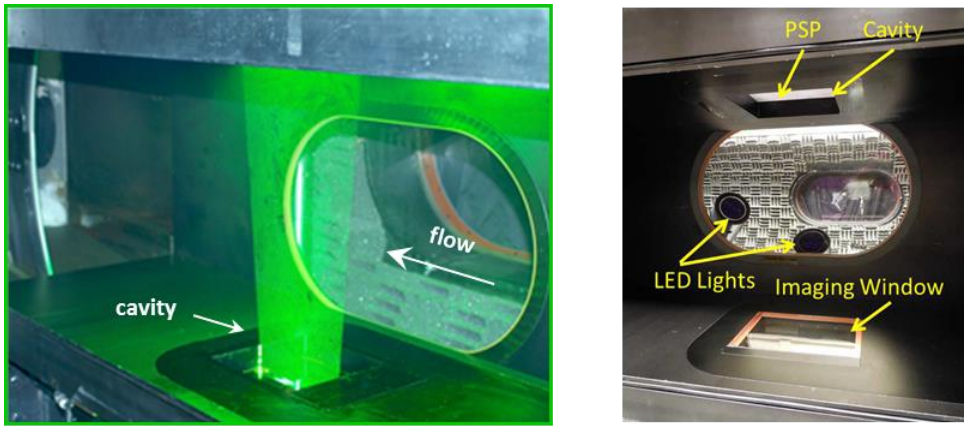

Fig. 1 Cavity photos: (a) cavity in the lower wall of the test section and the PIV laser sheet, and (b) cavity installed in the upper test section wall for PSP experiments.

C. Unsteady Pressures

Eight dynamic pressure sensors (Kulite XCQ-062-30A or similar) having a range of about 207 kPa and a flat frequency response up until about 50 kHz were placed in the cavity fore wall and the cavity aft wall. The sensors were located along the span of the walls, though only data at $z = 0$ is used for analysis here. The sampling frequency was 200 kHz and the data were lowpass-filtered at 50 kHz. Previous experiments have confirmed the experiments to be repeatable having a precision uncertainty on the mean of about 0.5% [2].

High-frequency PSP from Innovative Scientific Solutions, Inc. (ISSI) was sprayed onto the entire floor of the cavity (Fig. 1b). The paint used a platinum-tetra-fluoro-pheynl-porphyrin (PtTFPP) luminophore added on top of a porous ceramic binder. The porosity of the base layer added surface area to allow fast response of the paint. Specifically, a frequency response of approximately 10 kHz [34] was possible making it essentially time-resolved for resonance dynamics characterized herein. Moreover, the paint measurements have been shown to be in good agreement with pressure sensors [34].

Three ISSI LM2XX-DM-400 water-cooled light arrays excited the PSP over a range of about 400 nm ± 30 nm. The lights were placed in the plenum surrounding the tunnel to locate them as close as possible to the cavity. The majority of emission from the paint was centered at a wavelength near 650 nm. A high-speed camera (Photron SA-Z) fitted with a 50-mm lens was used to acquire full-view images of the cavity at framing rates of 20 kHz. The camera had a resolution of 1024 x 1024 pixels and a quantum efficiency of 49% at 630 nm. A 590 nm long-pass filter removed the 400 nm excitation light.

Raw images were post-processed using an adaptive Wiener filter in Matlab. This acted as a low-pass filter to reduce additive noise in the images. Static calibrations were used to convert the intensity ratios to pressure ratios, yielding the unsteady pressure fluctuations within the cavity. Additional details on the calibration and TR-PSP setup can be found in Casper et al. [34].

D. Time-Resolved Particle Image Velocimetry

Seeding was provided by a smoke generator that delivered a large quantity of mineral oil particles to the tunnel stagnation chamber. Measurement of the particle response across a shock wave has shown the particle size to be about 0.8 μm, which returns Stokes numbers of about 0.04 based on *a posteriori* measurements of typical cavity shear layer eddies. The particles, therefore, rapidly attain the local velocity even in the presence of velocity gradients in the shear layer [38]. Visual inspection of the PIV images showed adequate seeding in all portions of the cavity, including the recirculation region.

A quasi-continuous burst-mode laser (QuasiModo-1000, Spectral Energies, LLC) with both diode and flashlamp Nd:YAG amplifiers was used to produce a high energy pulse train at a wavelength of 532 nm. The laser design is based on a master oscillator power amplifier architecture and is similar to previously reported pulse-burst lasers [39-40]. As detailed in [32], the laser is capable of producing doublets with the variable inter-pulse spacing time and at varying pulse frequencies (repetition rates). Here, the laser was operated at 37.5 kHz with doublets separated in time by 3 μs. A 10.2 ms burst was generated every 8 seconds and the energy per pulse was about 27 mJ. Five bursts per wind tunnel run brought the total number of independent bursts (independent time-series) per condition to 245. The beam was shaped into a laser sheet covering the streamwise length of the cavity having a spanwise thickness of 1.5 mm, and was located at the spanwise center of the cavity.

Images were acquired using two high-speed cameras (Photron SA-Zs). Each camera was operated at 75 kHz at a resolution of 640 × 360 pixels. The two pulses in a doublet were frame-straddled around the inter-frame transfer time of the cameras to produce separate images for cross-correlation analysis. As a result, the PIV repetition rate was half that of the framing-rate, or 37.5 kHz. In a manner similar to Beresh et al. [32], the two cameras were angled downward at 12 degrees to peer into the cavity and placed side-by-side to extend the field of view in the streamwise direction. The combined field-of-view was about 120 × 30 mm. The cameras imaged about 50% of the cavity depth in contrast to the 100% depth covered in previous 10-Hz stereoscopic PIV experiments, which utilized a mirror in the test section plenum to increase optical access [12].

About 120,000 vector fields were acquired in total. However, since the vector fields within a 10.2 ms burst were correlated in time, the number of independent data sets corresponds to the total number of bursts used, namely 245. The image pairs were processed using the LaVision PIV software package DaVis v8.2 to a final interrogation window size of 24 × 24 pixels in the same fashion as described in Beresh et al. [32]. Finally, resonance dynamics as determined from the TR-PIV are compared to those given using a previous 10-Hz dataset [12].

E. Analysis Methods

Power spectral density (PSD) spectra of the PSP data and pulse-burst velocity data were computed using the Welch windowing algorithm in Matlab. Spatial distributions of the PSD amplitude at frequencies corresponding to cavity tones are shown herein to highlight the spatial variation associated with resonance in both the pressure (TR-PSP) and velocity (TR-PIV) fields. The frequency resolution of the TR-PSP and TR-PIV PSDs was 50 Hz and 100 Hz, respectively.

Joint-time frequency analysis (JTFA) on the time-resolved data was conducted using a wavelet transform. This technique shows the frequency content of the disturbances as a function of time, and has been used in other unsteady applications such as wake transition, meteorological studies, and cavity flows [21, 41-43]. The transform provides good time resolution for identifying intermittent mode-switching within the cavity. The wavelet transform was computed using a Matlab script provided in Ref. [43] with a Morelet mother wavelet.

The time-resolved velocity fields were bandpass-filtered in the time domain about each of the first three cavity tone frequencies using a Butterworth filter based on the algorithm in Russell [44]. This algorithm uses a cascade of first order filters and hence is precise for narrow band applications. The filter results in very little signal attenuation at the desired frequency band and is designed to produce zero phase-shift. A bandwidth of 100 Hz was chosen to narrowly focus on the resonance frequencies. An 'active' mode is defined to occur when the amplitude of the velocity measured is in the top forty percent in comparison to all the samples. Modes two and three used a location of $x = 3.6D$ and $y = 0.1D$ as the conditioning location, whereas mode one utilized a point above the cavity ($x = 2D$ and $y = 0.6D$) to remove the influence of broadband contributions on the analysis. This leaves about one-hundred cases of active modes for subsequent spectral and cross-correlation analysis.

Cross-correlations between velocity time sequences at points separated by fixed streamwise distance were computed allowing for the streamwise convection velocity U_c between the points to be calculated. The convective velocities were computed using the time delay corresponding to maximum correlation and the known distance between measurement locations. The analysis was performed in a row-by-row fashion, at every point within the row, thereby revealing spatial distributions of streamwise convective velocity. This methodology captures U_c over the entire measurement domain, though the data are essentially smoothed by a moving-average, lowpass filter.

The cross-correlation analysis was performed on the raw, unfiltered velocity data as well as the bandpass-filtered data. The streamwise separation between measurements locations was varied between ten and twenty vector spacings (0.45*D* – 0.90*D*). A spacing less than about ten vectors was generally too low for the temporal resolution of the measurements, whereas a spacing greater than about twenty vectors overly smoothed the convective velocity fields. Comparisons between calculations using separations within this range typically fell within the precision uncertainty of the measurements quantified in the results. Hence, the smaller spacing of 0.45*D* was utilized to maximize spatial resolution with one exception being the unfiltered case where a larger spacing of 0.68*D* was used to eliminate a non-physical jump in U_c observed at the interface between the two side-by-side measurements.

III. Results

A. Mean Flow and Pressure Spectra

The mean flow field over nearly the entire height and length of the cavity, obtained from 10-Hz, stereoscopic PIV measurements [12], is shown in Fig. 2a. The flow demonstrates the expected behavior of a mixing layer that grows with streamwise distance. A single recirculation region centered at about x/D = 3.4 is also evident. Below the cavity lip line (y = 0), the flow is turned downward in the mixing layer resulting in impingement on the aft wall.

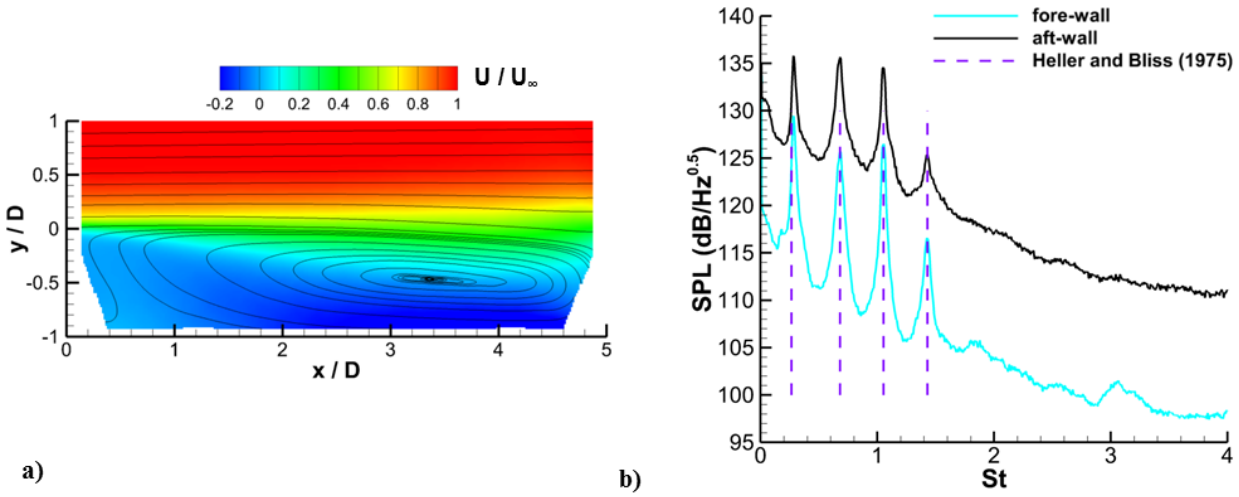

Fig. 2 Basic cavity flow properties: (a) mean streamwise velocity *U* contours with superposed streamlines [12], and (b) Sound pressure level spectra *SPL* at the fore wall and aft wall of the cavity. Dashed lines represent frequencies predicted by the modified Rossiter relation of Heller and Bliss [45].

Sound pressure level *SPL* spectra obtained at the fore wall and aft wall of the cavity are shown in Fig. 2b. At Mach 0.94, the first three Rossiter modes have similar amplitude. A fourth cavity tone is also observed and is omitted for brevity as its behavior is consistent with modes two and three. The expected frequencies of the cavity tones can be given with the Rossiter relation modified by Heller and Bliss [45]:

$$St = \frac{f_m L}{U_\infty} = \frac{m - \alpha}{\left[M_\infty \left(1 + \frac{\gamma - 1}{2} M_\infty\right)^{-1/2} + \frac{1}{\kappa} \right]} \qquad (1)$$

where f is frequency, m is integer mode number, U_∞ is freestream velocity, and γ is the ratio of specific heats. This semi-empirical equation is based on the assumption that vortical disturbances associated with resonance propagate downstream at a constant convection velocity of $\kappa \times U_\infty$. When a disturbance reaches the aft wall, there is a phase lag α (in fractions of a wavelength), which occurs before an upstream propagating disturbance is formed. According to this view, the upstream-propagating disturbance then moves at the speed of sound based on the stagnation temperature a_0. Throughout the literature, commonly used constants for phase lag and convective velocity are 0.25 and 0.57, respectively [10, 36]. Although the semi-empirical relation is a simplification of the cavity resonance physics (e.g., it is known that disturbances in the shear layer do not move at constant velocity [22, 26]), it often

provides good predictions of cavity tone frequencies. The current work is no exception. For instance, as shown in Fig. 2b, using the common values for α and κ gives agreement between the measured and predicted frequencies to within 2%.

B. Coherent Resonant Structures based on 10-Hz PIV

Coherent flow structures during resonance, based on previous 10-Hz PIV data [12], are first briefly presented and are later compared to structures obtained by bandpass filtering the TR-PIV data. To conditionally average the PIV in this case, a wavelet transform was used to bandpass filter the pressure sensor traces. This was achieved by setting wavelet transform coefficients other than those at the cavity tone frequencies to zero and then computing an inverse wavelet transform. This effectively bandpass filtered the pressure data, importantly, without a time delay to maintain synchronization with the 10-Hz PIV data. The conditional averaging was performed using the pressure data from the sensor installed in the center of the fore wall where turbulent fluctuations are smaller in comparison to the aft wall. Here, instances when a given cavity mode was active and the pressure measured at the upstream sensor was at a peak or a trough were used to produce phase-averaged vector fields. About ten percent of the available vector fields were used for each phase-averaged result. Finally, the mean wall-normal velocity field V was subtracted from the phase-averaged field V_θ to reveal the coherent flow structure [46] associated with resonance tones.

Coherent wall-normal velocity fields ($V_\theta - V$) corresponding to resonance modes two and three are shown in Fig. 3. As expected, moving from the case when the modal pressure is at peak (θ = 90 degrees) to when it is at a trough (θ = 270 degrees) results an in a velocity sign inversion. The coherent velocities show a spatial modulation in structure size with streamwise distance. For instance, the mode two fields show a significant growth in coherent structures to occur in the vicinity of $x = 3D$, while a decrease in structure size occurs in the aft end of the cavity for $x > 4D$. Modulation is also seen for mode three, particularly at θ_3 = 270 degrees, where structure size increases in the region $1D < x < 2D$ and in the region $3D < x < 4D$. The observations are explained subsequently using the TR-PIV data.

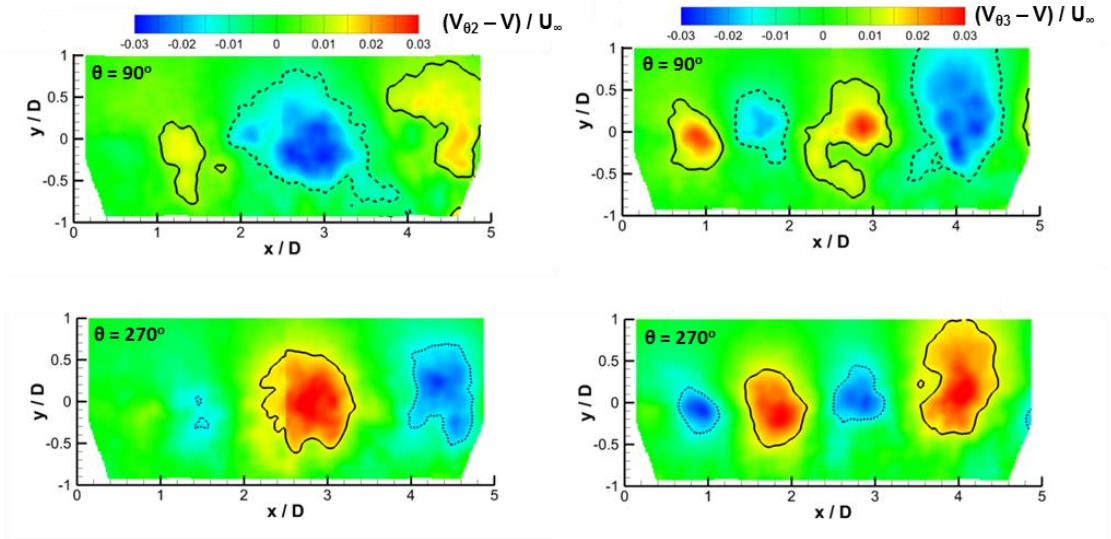

Fig. 3 Coherent flow structures ($V_\theta - V$) obtained with phase averaging of 10-Hz PIV data: mode two (left), and mode three (right).

C. Modulations of Cavity Pressure and Velocity

The dynamic events during cavity flows do not occur uniformly with time. Rather, modal amplitudes vary temporally through mode-switching [20-29 27, 29, 47]. Examples of this tonal modulation are shown in Fig. 4, which gives the time-varying frequency content of pressure measured at the fore wall during two separate wind tunnel experiments. Dashed lines appear in the figure to mark the first three cavity mode frequencies (f_1, f_2, and f_3). Though modulated differently, the first cavity mode is fairly active in both subfigures. Modes two and three, however, show substantial differences. For example, mode two is more active in Fig. 4a, whereas mode three is more active in Fig. 4b.

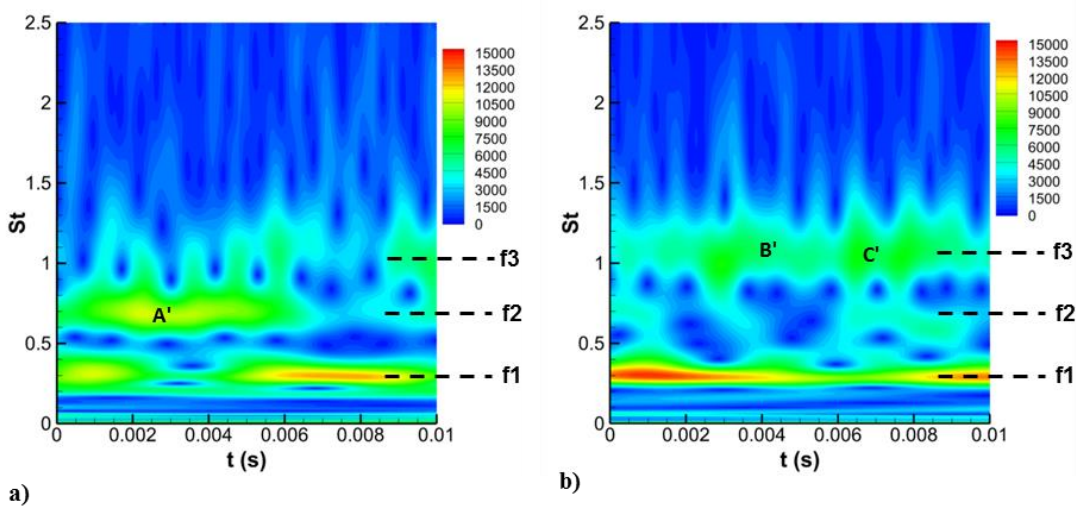

Fig. 4 Time-frequency content of fore wall pressure from two separate Mach 0.94 time sequences. Contour levels are amplitude of the wavelet transform with arbitrary units.

The corresponding variation of frequency content in the time-resolved velocity data is shown in Fig. 5. The JTFA was performed on the wall-normal velocity component v at a location of $x = 3.6D$ and $y = 0.1D$ where modes two and three were observed to be quite active in the bandpass-filtered v fields. The left subfigure corresponds to the same time sequence of Fig. 4a and the right subfigure corresponds to that in Fig. 4b. Similar to the pressure frequency content, the third cavity tone is observed to be much more active in the right subfigure than in the left. Also, like the pressure data, mode two contains greater fluctuations in the left subfigure. In both Fig. 4a and in Fig. 5a, mode two exhibits a peak around a time of 0.003 seconds (labels A and A'). Though less pronounced, some correlation between Fig. 4b and Fig. 5b can also be seen for the third cavity mode (B and C). On the other hand, the correlation between the pressure and velocity figures at f_1 is more limited, an observation which is revisited subsequently.

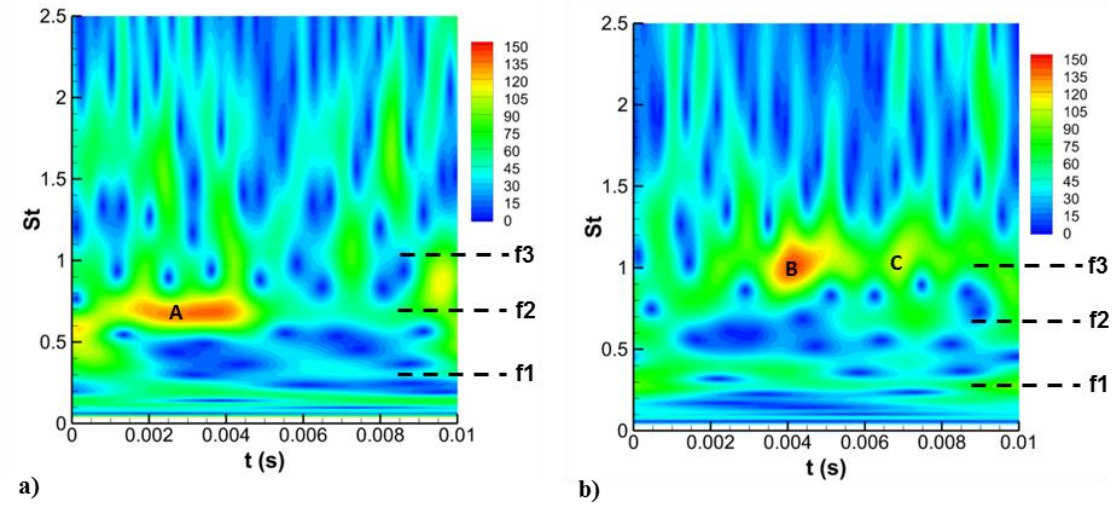

Fig. 5 Time-frequency content of vertical velocity at $x = 3.6D$ and $y = 0.1D$: (a) same time sequence as Fig. 3a, and (b) same time sequence as Fig. 3b. Contours are amplitude of the wavelet transform with arbitrary units.

D. Resonant Flow Structure based on TR-PIV

To characterize resonance dynamics, the pulse-burst PIV data were bandpass filtered about the modal frequencies. This allows for the contributions of each cavity mode to be separated and analyzed. As discussed subsequently, modes two and three show behavior more consistent with the classical view [1] that resonance occurs

in part through the downstream propagation of vortical disturbances. Thus, these modes are described prior to mode one.

An example flow structure during resonance is shown in Fig. 6, which gives the bandpass-filtered, wall-normal velocity v_{f2} (left) and streamwise velocity u_{f2} (right) fields corresponding to a cycle of mode two (St = 0.68) lasting for a period T_2. The figure was generated from a single experiment, namely the same as in Fig. 4a and Fig. 5a when mode two was active and is representative of other mode two cycles. The vertical velocities associated with mode two reveal a clear convection of organized structure as time increases. At t = 0, a region of organized positive vertical velocity appears near $x = D$ (label A). With continuing time, this structure convects downstream reaching a position near x/D = 3.4 at $t = 0.87T_2$. Upon completion of a full cycle at T2 (not shown) it is apparent that the upstream region of positive vertical velocity (A) moves downstream to become the larger region of positive vertical velocity (A'). Similar observations are seen in the regions of negative vertical velocities (B and B').

The streamwise modal velocities exhibit a more complex flow structure than the vertical. A region of negative velocity tends to reside below a region of higher velocity and vice-versa, an observation consistent with the classical view of propagating vortical structures. As the flow structures propagate from the upstream portion of the cavity to the streamwise center, they also appear to grow in the upstream direction ($t = 0.17T_2$ and $t = 0.70T_2$, e.g.). As discussed in Larchevêque et. al [22], this upstream growth is likely related to the fact that the streamwise velocity in cavity flows tends to be more strongly correlated to the pressure waves associated with resonance. In other words, the upstream growth is most likely is related to the propagation of pressure waves and not advection of vortical flow structures. Regardless, similar to the wall-normal component, an overall downstream convection of negative (C and C') and positive velocities (D and D') is also observed in the streamwise velocities.

Inspection of Fig. 6 also reveals a modulation of structure size with streamwise distance. For instance, in the wall-normal fluctuations, the structures are largest near $x = 3D$ ($t = 0.35T_2$ and $t = 0.87T_2$, e.g.). Additionally, the structures undergo more rapid changes in height near this location as annotated in the $t = 0.35T_2$ and $t = 0.87T_2$ subfigures. This rise and fall of flow structures tends to occur in vicinity of the mean recirculation region centered near $x = 3.2D$ (Fig. 2a). A modulation of structure size with streamwise location is also seen in the streamwise velocities.

Bandpass-filtered velocities corresponding to a mode three cycle (St = 1.04) of resonance having period T_3 are displayed in Fig. 7. The figure was generated from the same time sequence as in Fig. 4b and Fig. 5b when mode three was active and is representative of other mode three cycles. Like mode two, an obvious convection of wall-normal flow structures is seen with increasing time, though as expected, the structures are smaller and more closely spaced, consistent with a lower wavelength. Once again, regions of opposite signed velocity appear under the structures propagating in the shear layer. Again this observation is related to the fact that pressure disturbances propagate through vorticity as is emphasized with the annotations in the $t = 0.21T_3$ subfigures.

As the structures propagate downstream they grow in size and reside at higher wall-normal locations within the cavity. A similar upward trajectory of resonant flow structures has been observed in several incompressible [48, 49], and compressible [50] numerical studies. A possible explanation for this observation is that vortices higher in the shear layer will be less susceptible to being interrupted by the recirculation region. Thus, a structure at a greater y/D may be statistically more likely to remain intact with downstream propagation.

The growth in structure size does not occur uniformly in the streamwise direction. In the case of the streamwise velocities, a spatial modulation of structure size is observed near $x = 2D$ and $x = 4.2D$, where the structures traveling within the shear layer (i.e., the annotated structures) tend to be largest. In the wall-normal velocity subfigures, pronounced structure growth occurs at approximately $0.5D < x < 2.4D$ (structure A t = 0 to $1.07T_3$) and at $3D < x < 4D$ (structure A $t = 0.21T_3$ to $0.64T_3$). This modulation of wall-normal structure size is summarized in Fig. 8a where flow structures from each measurement time in a mode three cycle (Fig. 8a) are superposed. The aforementioned regions of structure growth are clearly apparent and a decrease in structure size is also evident in the region $2.4D < x < 3D$. The streamwise modulation of mode two is summarized in Fig. 8b, which plots lines of constant wall-normal velocity ($0.017U_\infty$) at each available measurement time of the cycle shown in Fig. 6. This effectively captures the envelope of resonant flow structure size during an entire cycle. Similar to Fig. 6, the structure size is observed to peak near $x = 3.4D$ before decreasing as the aft-wall approached.

In Fig. 6, the wall-normal velocity at a time of $0.70T_2$ closely resembles the phase-averaged result corresponding to mode two at θ_2 = 270 degrees in Fig. 3. In both cases a large region of positive velocity resides near $x = 3D$ and a region of negative velocity is seen near the aft end of the cavity. Similarly, in Fig. 7, the wall-normal velocity at a time of $0.86T_2$ closely resembles the result at θ_2 = 270 degrees in Fig. 3. Each of these cases was averaged over the wall-normal coordinate to produce the comparison shown in Fig. 9. In the case of both mode two (Fig. 3a) and mode three (Fig. 3b) the independent methods produce reasonable agreement indicating that either is well suited to produce coherent structures associated with resonance.

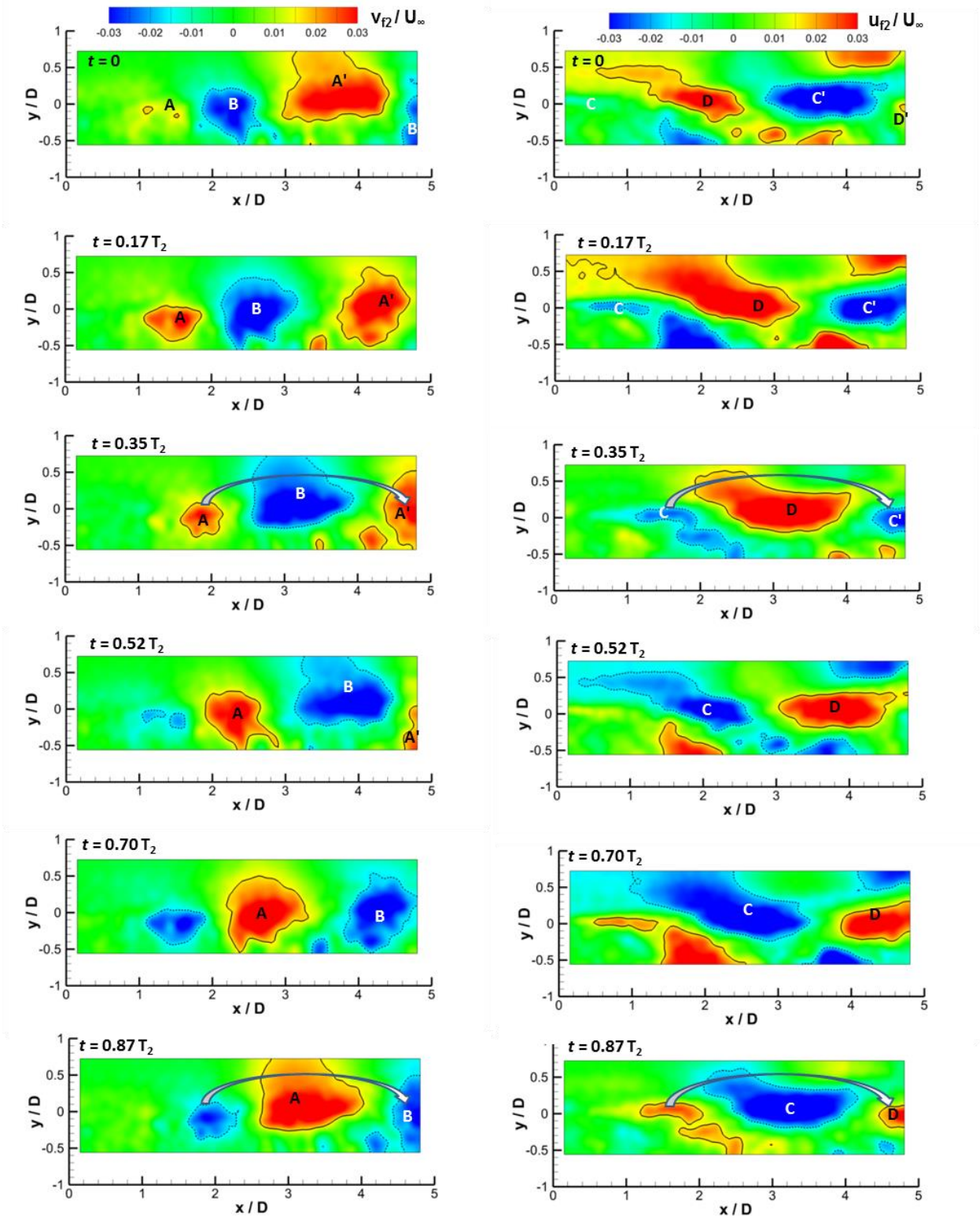

Fig. 6 Mode two (*St* = 0.68) bandpass-filtered velocities: wall-normal (left), and streamwise (right). Solid and dashed lines correspond to 0.017U_∞ and -0.017U_∞, respectively.

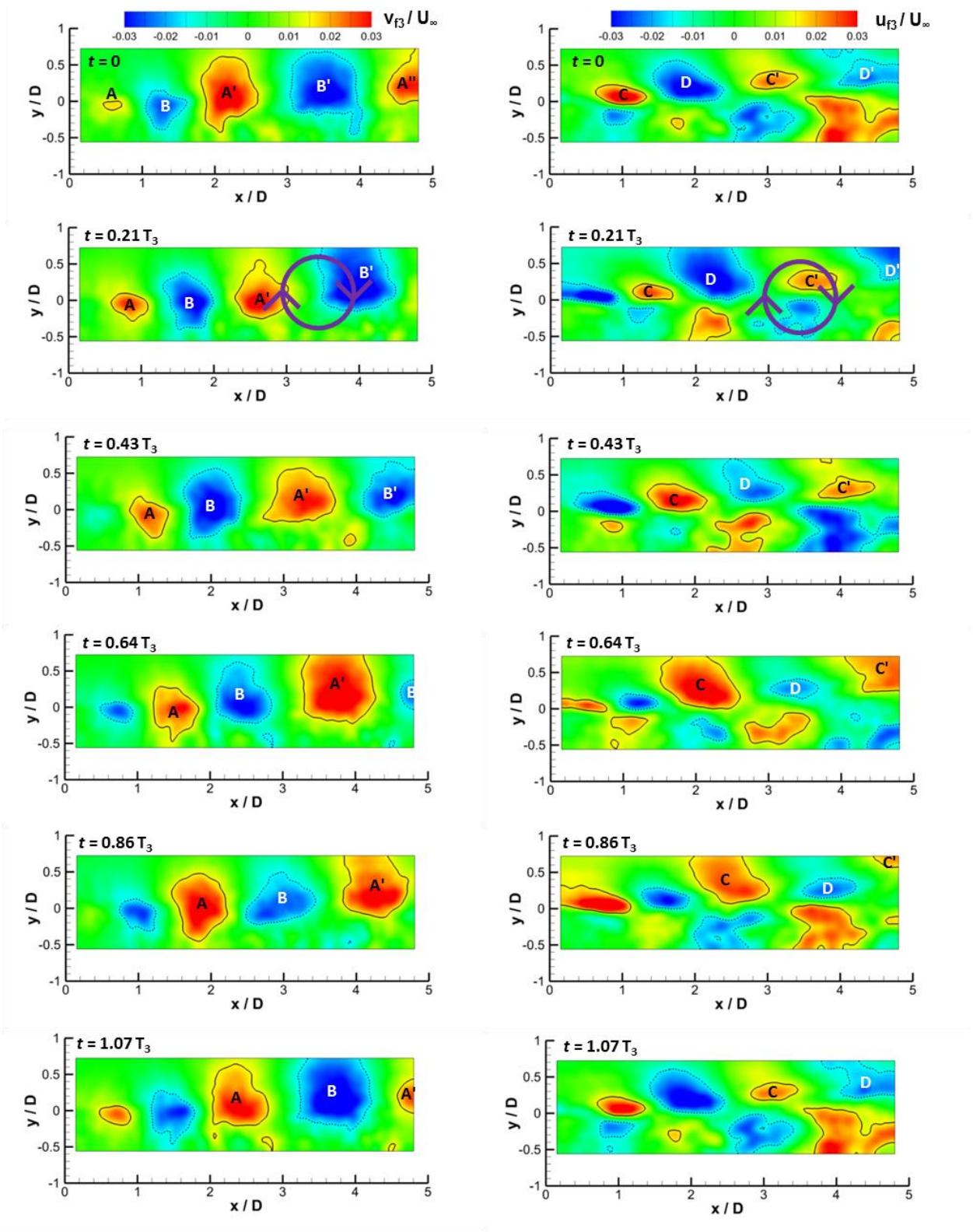

Fig. 7 Mode three (*St* = 1.04) bandpass-filtered velocities: wall-normal (left), and streamwise (right). Solid and dashed lines correspond to 0.017U_∞ and -0.017U_∞, respectively.

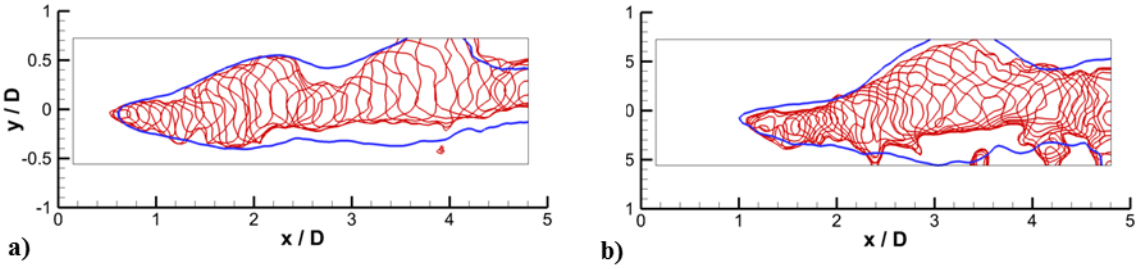

Fig. 8 Streamwise modulation of wall-normal resonant flow structures: (a) mode three, and (b) mode two. The red contours in each figure are lines of constant $0.02U_\infty$ showing superposed structures and the blue contours are lines of constant wall-normal velocity PSD amplitude ($0.002\ \mathrm{Hz}^{-0.5}$).

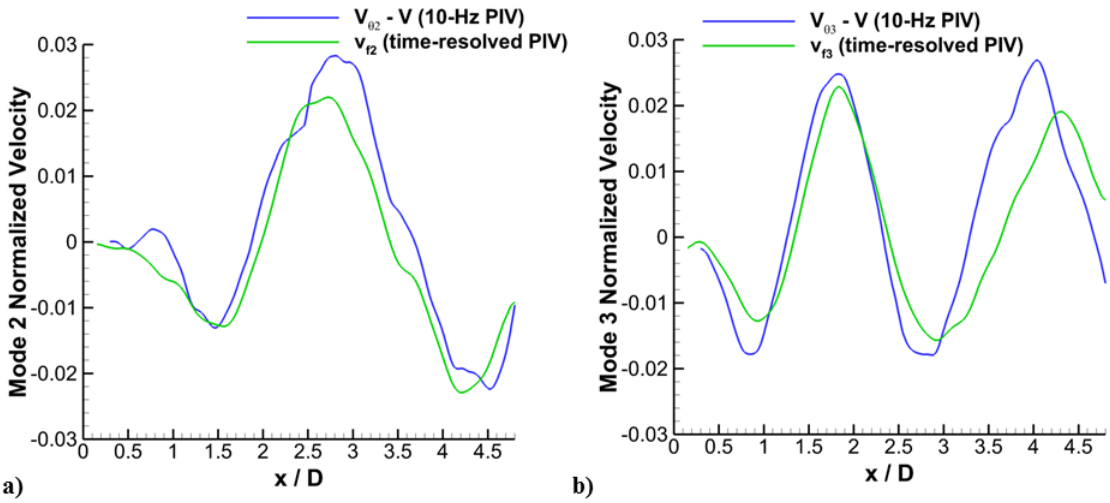

Fig. 9 Modal wall-normal velocity fluctuations, normalized by U_∞, obtained from bandpass filtering the TR-PIV data and those found by phase-averaging previous [12] 10-Hz PIV data: (a) mode two, and (b) mode three.

Bandpass-filtered velocity fields corresponding to cavity mode one (St = 0.28) are displayed in Fig. 10. The time sequence was obtained during the same experiment as in Fig. 5b, when mode one was active. Like modes two and three, a convection of wall-normal flow structure is evident. As time progresses through the full cycle period T_1, the regions of positive (A) and negative (B) wall-normal velocity move downstream. A major difference with respect to the two higher frequency modes, however, is that this convection takes place at a lower wall-normal location. In fact, comparison to the mean flow field in Fig. 2 suggests that wall-normal flow structures are moving through a region in the shear layer more influenced by recirculation.

A convection of resonant flow structure is also seen in the streamwise filtered velocity u_{f1}. As time progresses, regions of negative (C) and positive (D) streamwise velocity propagate downstream once again lower in the cavity. In comparison to the wall-normal modal velocities, however, the streamwise velocities exhibit larger variations above $y = 0$. For instance, at $t = 0.20T_1$, a large region of positive velocity extends across the cavity length. A similar instance of a large negative velocity region can also be seen at $t = 0.60T_1$. These regions were observed to occur with downstream propagation beginning at the upstream limit of the measurement domain. The velocity fluctuations are perhaps related to a large-scale flapping of the shear layer that has been observed in several incompressible [28, 53-56] and compressible [36] cavity flows. This flapping has been suggested to be associated with low-frequency dynamics in the recirculation region [53-56]. Additionally, for $St < 0.5$, Liu and Katz [28] show the flapping to stem from oscillations in the boundary layer upstream of the cavity, which could explain the large-scale streamwise velocity fluctuations seen here at $y > 0$. Moreover, fluctuations upstream of the cavity would be consistent with the fact that wavelength of mode one is greater than the length of the cavity. Also similar to herein (Fig. 10), Liu and Katz [28] noted the flapping to be much more readily apparent in the streamwise velocities in comparison to the wall-normal.

Many of the preceding observations related to the bandpass-filtered velocity fields can be summarized concisely with spatial distributions of PSD amplitude at the given cavity mode frequencies. Along these lines, PSD amplitude distributions of wall-normal and streamwise velocity at frequencies corresponding to cavity modes one through three are shown in Fig. 11. In the case of mode one (Fig. 11a and Fig. 11b), the PSD peaks lie near the recirculation region (Fig. 2a). As the cavity mode number increases from one through three, the extent of resonance activity grows to reach higher portions within the flow. Such an observation is consistent with the bandpass-filtered results, which in general showed that resonant flow structures propagated at higher wall-normal locations as the mode number was increased.

As the mode number increases, the spatial wavelength observed in the PSD distributions decreases, implying that the streamwise variation typically observed in cavity pressures also appears in the modal velocity fields. Kegerise [20] also noted a spatial periodicity in modal velocities and densities using hot wire and optical deflectometry measurements. A wavelength is apparent in both velocity components, although, in general, the streamwise PSDs exhibit a more complex, height-dependent variation like their bandpass-filtered counterparts. Finally, the streamwise undulations in PSD amplitude are consistent with locations in the bandpass-filtered velocities where coherent structures were observed to undergo more rapid changes in size, particularly at modes two and three. To emphasize this, lines of constant PSD amplitude capturing the PSD undulations are also plotted in Fig. 8. It is clear that the periodicity observed in the modal velocity fields occurs with a streamwise modulation of resonant coherent structure size. Importantly, since this modulation represents a variation in velocity fluctuations, this implies that the periodicity observed in the filtered velocity fields and PSDs are primarily tied to cavity acoustics, an observation which is quantified subsequently.

E. Time-Resolved Surface Pressures

Surface pressure distributions along the cavity floor given from the TR-PSP are presented in Fig. 12a - Fig. 12c. The PSD amplitudes at the cavity resonance frequencies are used to plot the spatial distributions. Note that the lines at $z / D = -1.8$ and the semicircles near $z / D = -2.5$ are measurement artifacts and do not represent actual pressure variations. Overall, the pressure distributions are fairly one-dimensional and show little variation in pressure fluctuations across the spanwise dimension of the cavity. Like the velocity PSDs, the spatial wavelengths of the pressure fields decrease with mode number. For instance, the mode one distribution exhibits a single minimum near $x = 2D$, whereas modes two and three have two and three local minima, respectively.

The streamwise variation of PSD amplitude at the spanwise center of the cavity is plotted for modes one (Fig. 12d), two (Fig. 12e), and three (Fig. 12f). Several previous cavity studies have observed similar spatial distributions in pressure, which look similar to patterns produced by standing waves [10, 33, 34, 51, 52]. However, these spatial amplitude variations can be better explained using Rossiter's model of cavity resonance which consists of downstream-propagating shear layer disturbances and weaker upstream-propagating acoustic waves. Casper et al. [34] recently showed that spatial amplitude variation associated with resonance tones can be well represented by the superposition of two sine waves traveling at speeds used in the Rossiter relation. Because the upstream-propagating and downstream-propagating waves have different speeds and amplitudes, a standing wave is not generated. However, an interference pattern is developed by the wave superposition. The envelope of that interference pattern results in minima and maxima, which matches the observed spatial distribution in the pressure PSDs at each mode. Importantly, the minima and maxima do not move with time since the group velocity of the wave summation is zero, i.e. fixed within the cavity, because the interfering waves have the same frequency [34]. As a result, the periodic pressure distributions seen in Fig. 12 and elsewhere are produced.

F. Relationship between Surface Pressures and Velocity Fields

Of prime importance is how the velocity field is coupled to the pressure field. To estimate the integrated behavior across cavity height, the streamwise velocity PSDs were averaged across the entire wall-normal extent of the measurement region. The resulting averaged profiles corresponding to modes one, two and three are also shown in Fig. 12. In the case of modes two (Fig. 12e) and three (Fig. 12f), the locations of local minima in the pressure PSDs correspond to local maxima in the streamwise velocity PSDs. Similarly, local maxima in the pressure PSDs correspond to local minima in the streamwise modal velocities. Because the streamwise modal pressure distributions have fixed local minima and maxima [34], these observations can be explained with analogy to a standing wave, where nodes in pressure correspond to antinodes in streamwise velocity, and vice-versa. In other words, the very same constructive and destructive interference responsible for the periodic pressure distributions is apparent in the velocity fields consistent due to cavity acoustics.

Wall-normal modal velocity PSDs averaged across the measurement height are also plotted in Fig. 12. At modes two and three, the wall-normal distributions take on a wave-like form similar to the streamwise distributions. Since

cavity resonance occurs with the propagation of vortical structures, a coupling between the streamwise and wall-normal velocity fluctuations through rotation is to be expected. Though in close proximity, local wall-normal velocity maxima no longer occur at the location of pressure minima. Rather, the wall-normal waveforms precede the streamwise waveforms in x. This is also consistent with the propagation of vortical structures, where regions of upwash precede streamwise velocity variations (Fig. 7, $t = 0.21T_2$, e.g.).

At first glance, the relationship between surface pressure and modal velocities within the cavity at mode one (Fig. 12d) is apparently unlike modes two and three. Rather than exhibiting a local maximum at the local minimum in pressure, the velocity PSDs have an increasing amplitude with streamwise distance and contain maxima further downstream near $x = 4.2D$. As detailed in Beresh et al. [57], the modal velocity PSDs contain contributions from resonance as well as random fluctuations. At some cavity locations, resonant velocity fluctuations at mode one can be overwhelmed by broadband components.

To further investigate mode one acoustics, PSDs of wall-normal velocity at five points within the cavity are shown in Fig. 13a. For locations at $y = 0$ or lower, peaks corresponding to mode one tend to have little prominence. In fact, in the recirculation region ($x = 4D$ and $y = -0.3D$), broadband fluctuations have completely overwhelmed any evidence of a peak at f_1. On the other hand, the points above $y = 0$ do show evidence of mode one in the spectra. This is quantified further in Fig. 13b where mode one velocity PSD distributions, averaged across the upper portion of the measurement domain ($y > 0$), are compared to the pressure distribution. In this regime, cavity acoustics are evident as local maxima in both the streamwise and wall-normal velocities occur near the pressure minimum. The increasing velocity fluctuations at $x > 3D$ are likely explained by increasing turbulence as the aft wall is approached [12, **Error! Reference source not found.**, 58, e.g.]. Likewise, a diminishing contribution of mode one acoustics with increasing x is also observed in Fig. 13a in the spectra corresponding to $y = 0.6D$.

Since the mode one velocity PSDs do not readily exhibit peaks at locations lower within the cavity, it is difficult to determine the nature of the resonance using the time-resolved PIV data alone. On the other hand, conditionally averaging the 10-Hz PIV data based on mode one pressures should remove random fluctuations [46]. Along these lines, in a manner similar to Fig. 3, the coherent streamwise velocity fields ($U_{\theta 1} - U$) corresponding to mode one are shown in Fig. 14. Similar to the bandpass-filtered sequence in Fig. 10, mode one is seen to be active over the entire streamwise extent of the cavity length as well as in the recirculation region. Encouragingly, a similar conclusion can be reached by conditionally correlating the TR-PIV data to the pressure sensor data [57].

G. Convective Velocities

Convective Velocities Based on Unfiltered Velocity Data

The spatial distribution of convective velocity within the cavity using the unfiltered velocity data is displayed in Fig. 15a. The convection velocity was based on correlations of wall-normal velocity since v is less influenced by upstream-propagating pressure waves than u and is thereby more likely to give a better measurement of U_c [22].

The unfiltered convective velocity demonstrates expected trends. At a constant streamwise station, U_c increases with y. Moreover, at constant y, the convective velocity tends to increase with increasing streamwise distance. These trends are consistent with the mean flow field (Fig. 2), which shows the shear layer dives downward into the cavity with increasing streamwise distance. The convective velocity profile at $y = 0$ is plotted in Fig. 15b, where the precision uncertainty based on 95% confidence intervals is about $\pm 0.01U_\infty$. The convective velocity increases as x increases from $1D$ through $4D$. Over this same region, the slope of the profile decreases until a plateau region is reached between about $3D$ and $3.8D$. The convection velocity then begins to decrease for the rest of the measurement domain.

These measurements are in line with previous cavity flow studies. Hassan [26], for example, measured similar convective velocities in incompressible cavity flows, including a region of increasing slope, a plateau region, and a region of decreasing velocity following the plateau. The average convective velocities in Hassan [26] resided between about $0.40U_\infty$ and $0.50U_\infty$, similar to the values reported in the incompressible studies of Bian et al. [59] and Haigermoser et al. [60]. In comparison, in the available measurement region, the average convective velocity here computes to $0.48U_\infty$, well below the $0.57U_\infty$ used in the Rossiter relation to correctly predict the tone frequencies. The simulated convective velocity profile of Larchevêque [22], computed at similar flow conditions ($M_\infty = 0.85$, $L/D = 5$) to those herein, is also shown in Fig. 15. The current measurements show similar trends, although the simulated profile has an overall higher average convective velocity of $0.52U_\infty$. As discussed in Larchevêque [22], the relatively constant acceleration observed in the upstream portion of the cavity corresponds to a region where the flow is predominantly two dimensional, whereas the sudden decrease in the downstream portion is associated with the aft wall.

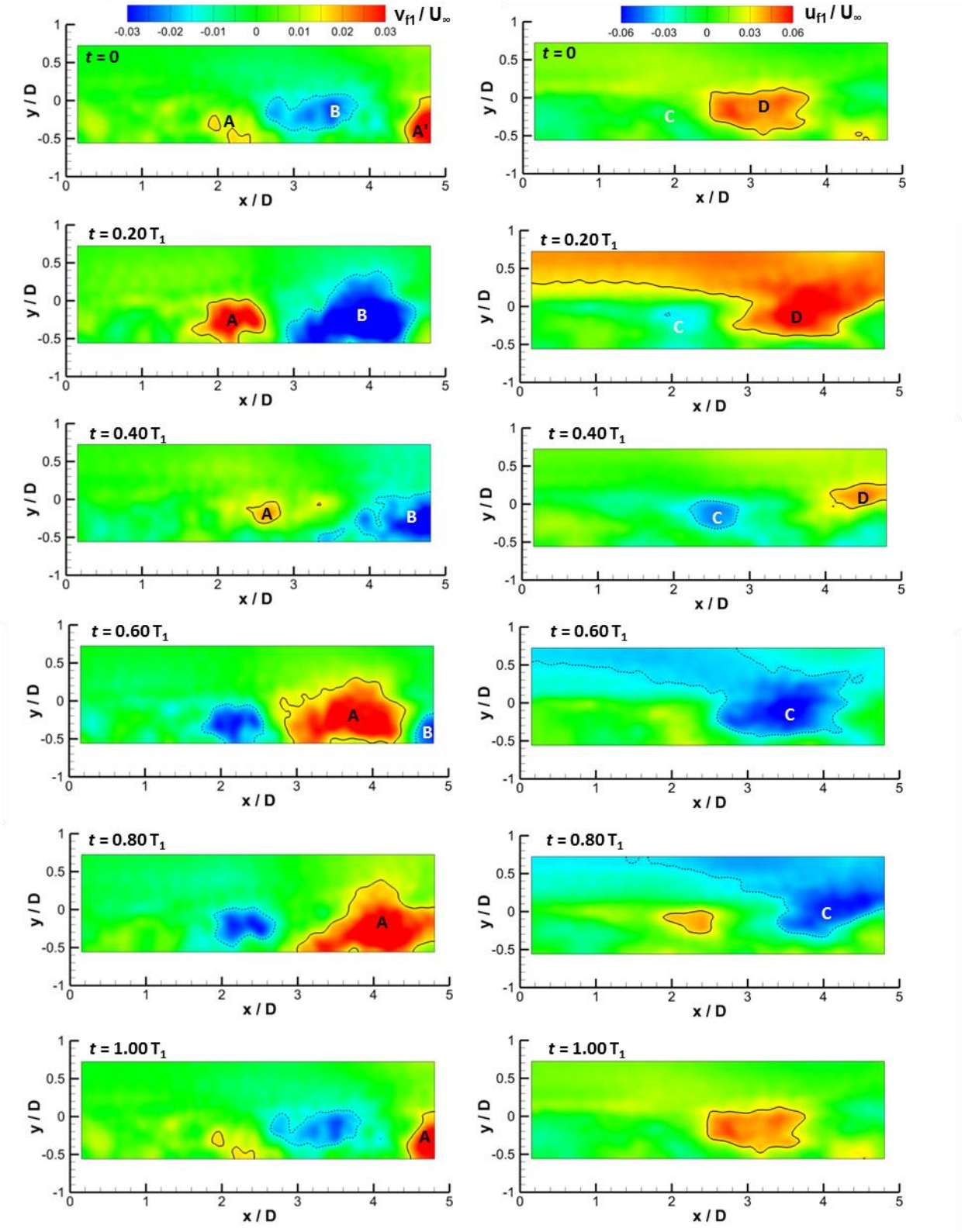

Fig. 10 Mode one bandpass-filtered velocities: wall-normal (left), and streamwise (right). Solid and dashed lines correspond to $0.017U_\infty$ and $-0.017U_\infty$ in the wall-normal subfigures and $0.034U_\infty$ and $-0.034U_\infty$ in the streamwise subfigures.

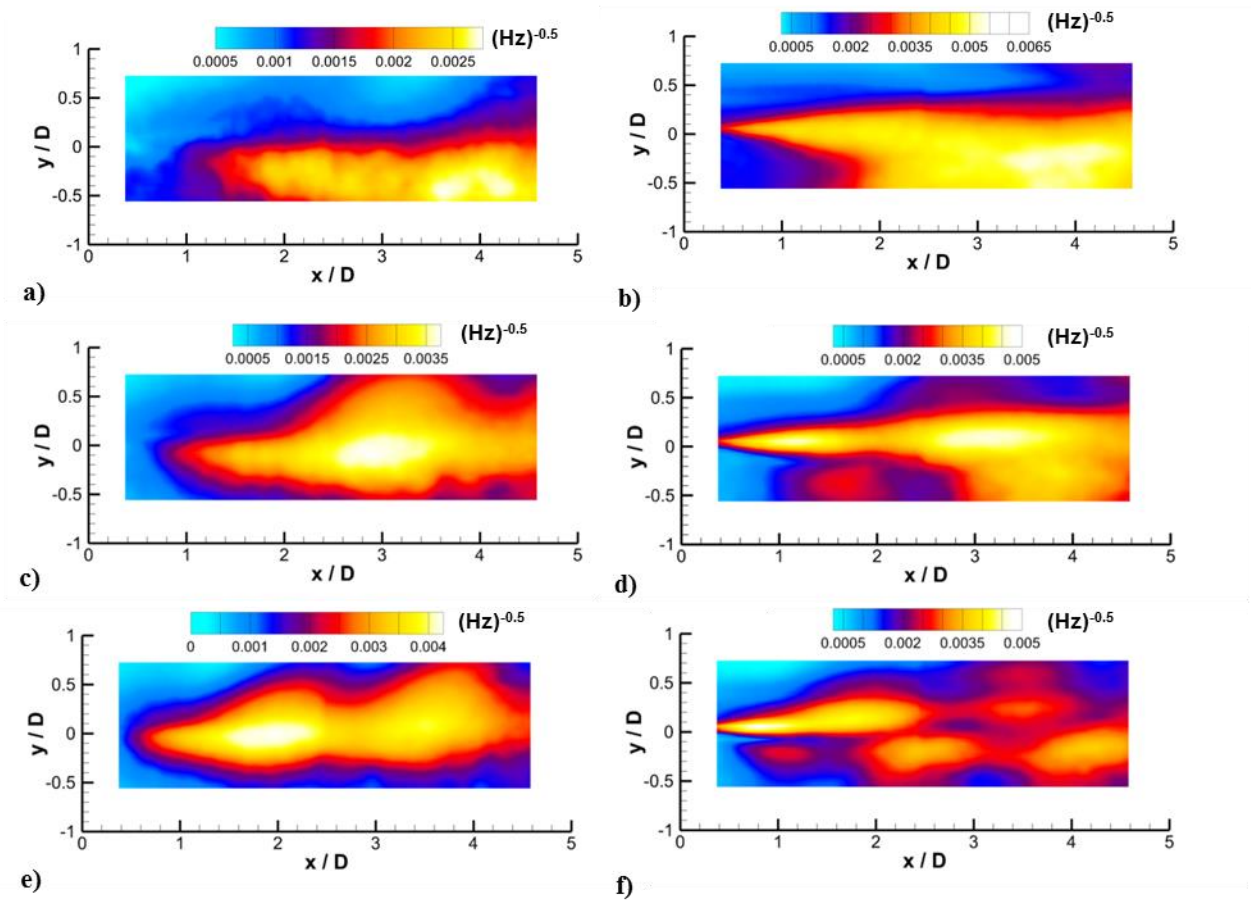

Fig. 11 Spatial distributions of velocity PSD amplitudes at the cavity tone frequencies normalized by U_∞: a) mode one, wall-normal, b) mode one, streamwise, c) mode two, wall-normal, d) mode two, streamwise, e) mode three, wall-normal, and f) mode three, streamwise

Modal Convective / Propagation Velocities

Modal convective velocities, based on the cross-correlation of bandpassed-filtered wall-normal velocity fields are shown in Fig. 16. The convective velocities associated with the bandpass-filtered vector fields present a unique view of resonance dynamics in cavity flows. Unlike the measurements of unfiltered velocity data shown here in Fig. 15 and in other studies [22, 26], a periodicity is observed in the bandpass-filtered velocities. There is a wavelength in the convective velocity, which decreases with increasing mode number in a fashion analogous to the decreasing spatial wavelengths in the modal velocity PSDs and the surface pressure PSDs.

Convective velocity profiles obtained at $y = 0$ for all three cavity modes are plotted in Fig. 16d. On average, the convective velocity increases with cavity mode number. Specifically, the average U_c of modes one, two, and three in the figure calculates to $0.13U_\infty$, $0.42U_\infty$, and $0.47U_\infty$, respectively. This is likely related to the fact that as the cavity mode number increases, the coherent structures tend to reside at higher locations within the flowfield reaching a higher portion of the shear layer where the mean convective velocity is higher (Fig. 2a). Likewise, when the mode number decreases, the resonance activity shifts to a region with locally lower mean velocity where a lower convective velocity would be expected.

The streamwise convective velocity distributions in Fig. 16d corresponding to modes two and three show a clear periodicity. Casper et al. [34] also measured a periodic convective velocity based on correlations of bandpass-filtered surface pressures using TR-PSP. Moreover, their wave interference model, based on Rossiter's interpretation of upstream-traveling acoustic disturbances superposed with downstream-traveling shear layer disturbances, predicted oscillations in convective velocity. The modal convective velocity exhibits periodicity because the superposed waves travel at different velocities and have different amplitudes. With this in mind it is more appropriate to refer to the distributions in Fig. 16 as modal propagation velocities. Here, the fact the modal

propagation velocity in the shear layer ($y = 0$) is positive for modes one through three indicates that the downstream-propagating disturbances overwhelm their upstream-propagating counterparts at this location.

A comparison of the propagation velocity, velocity fluctuations, and the surface pressures variations at modes two and three is shown in Fig. 17. As previously discussed, local minima in modal pressures correspond to local maxima in modal velocities with analogy to a standing wave. In the case of both modes, local maxima in propagation velocity reside at regions of locally increased modal velocity fluctuations. These regions occur at locations of maximum constructive interference in the velocity field. In contrast, the regions of diminished velocity fluctuations occur where the destructive interference is the greatest and result in decreased modal convective velocities.

IV. Conclusions

The unsteady resonance characteristics of Mach 0.94 flow over a cavity were explored with TR-PIV using a pulse-burst laser and surface pressure measurements using TR-PSP. These novel, time-resolved data allowed the cavity dynamics to be studied without phase or ensemble averaging. Modulations of the cavity velocity and pressure field consistent with mode-switching were observed.

The resonance dynamics of the first three cavity modes were probed with bandpass filtering, which was able to reveal the flow structure associated with each mode. The first Rossiter mode occurred through large-scale motions in the shear layer as well as near the recirculation region. The second and third modes contained organized structures consistent with convecting vortical disturbances in the shear layer. The size of the coherent structures changed periodically with downstream propagation, implying a streamwise modulation. A similar coherent flow structure pattern was found independently by conditionally averaging 10-Hz repetition rate PIV data.

The surface pressures displayed streamwise amplitude variations explained using Rossiter's interpretation, namely that cavity resonance consists of downstream-propagating disturbances in the shear layer and weaker acoustic waves propagating upstream. The locations of local minima in the surface pressure corresponded to local maxima in the modal streamwise velocity. Similarly, local maxima in the pressures corresponded to local minima in the streamwise modal velocities. These observations can be explained with analogy to a standing wave, where nodes in pressure correspond to antinodes in streamwise velocity, and vice-versa. Thus, the constructive and destructive interference responsible for the periodic pressure distributions was readily apparent in the velocity fields. Similar periodic distributions occurred in the wall-normal modal velocities. However, the wall-normal velocity waveforms preceded the streamwise velocity waveforms in space, an observation consistent with the downstream propagation of vortical structures.

Modal propagation velocities during cavity resonance were found with cross-correlations of the wall-normal, bandpass-filtered velocities. The convective velocities were found to decrease with decreasing mode number, consistent with modal activity residing in lower portions of the cavity where the local mean velocities were diminished. Like the modal velocities, the convective velocities associated with resonance were found to have streamwise wavelengths that decreased with increasing mode number. Such oscillations were also the result of constructive and destructive interference in the velocity fields.

Together the TR-PIV and TR-PSP measurements enabled the exploration of the resonant nature of compressible cavity flows. These powerful diagnostics demonstrated that many of the important resonance dynamics can be explained through straightforward acoustical analogies.

Acknowledgments

Wavelet software was provided by C. Torrence and G. Compo, and is available at URL: http://paos.colorado.edu/research/wavelets/. The authors thank Lawrence Dechant and Matthew Barone for helpful discussions on cavity physics.

References

[1] Rossiter, J. E., "Wind-Tunnel Experiments on the Flow Over Rectangular Cavities at Subsonic and Transonic Speeds," Aeronautical Research Council Reports and Memoranda, October 1964.

[2] Wagner, J. L., Casper, K. M., Beresh, S. J., Hunter, P. S., Spillers, R. W., Henfling, J. F., and Mayes, R. L., "Fluid-structure interactions in compressible cavity flows," *Physics of Fluids*, Vol. 26, No. 6, pp.066102.

[3] Barone, M., and Arunajatesan, S., "Pressure Loadings in a Rectangular Cavities with and Without a Captive Store, *Journal of Aircraft*, Vol. 53. No. 4, pp. 982-991.

[4] Arunajatesan, S., Ross, M., Barone, M., and Garret, T. J., "Validation of an FSI Modeling Framework for Internal Captive Carriage Applications," AIAA Paper 2013-2157.

[5] Wagner, J. L., Casper, K. M., Beresh, S. J., Hunter, P. S., Spillers, R. W., and Henfling, J. F., "Response of a Store with Tunable Natural Frequencies in Compressible Cavity Flow," *AIAA Journal*, Vol. 54, No. 8, 2016, pp. 2351-2360.
[6] Rockwell, D., and Naudascher, E., "Self-sustained oscillations of impinging free shear layers," *Annual Review of Fluid Mechanics*, Vol. 11, 1979, pp. 67-94.
[7] Rockwell, D., and Naudascher, E., "Review-Self Sustaining Oscillations of Flow Past Cavities," *Journal of Fluids Engineering*, Vol. 100, 1978, pp. 152-165.
[8] Rowley, C. W., and Williams, D. R., "Dynamics and Control of High-Reynolds-Number Flow over Open Cavities," *Annual Review of Fluid Mechanics*, Vol. 38, 2006, pp. 251-276.
[9] Cattafesta, L. N., Song, Q., Williams D. R., Rowley C. W., and Alvi, F. S., "Active control of flow-induced cavity oscillations," *Progress in Aerospace Sciences*, Vol. 44, 2008, pp. 479-502.
[10] Tracy, M. B., and Plentovich, E. B., "Cavity Unsteady-Pressure Measurements at Subsonic and Transonic Speeds," NASA Technical Paper 3669, December 1997.
[11] Beresh, S. J., Wagner, J. L., Pruett, B. O., Henfling, J. F., and Spillers, R. W., "Supersonic Flow over a Finite-Width Rectangular Cavity," *AIAA Journal*, Vol. 53, No. 2, 2014, pp. 296-310.
[12] Beresh, S. J., Wagner, J. L., Henfling, J. F., Spillers, R. W., and Pruett, B. O., "Width Effects in Transonic Flow over a Rectangular Cavity," *AIAA Journal*, Vol. 53, No. 12, 2015, pp. 3831-3835.
[13] Arunajatesan, S., Barone, M. F., Wagner, J. L., Casper, K. M., and Beresh, S. J., "Joint experimental/computational investigation into the effects of finite width on transonic cavity flow," AIAA Paper 2014-3027.
[14] Beresh, S. J., Wagner, J. L., and Casper, K. M., "Compressibility Effects in the Shear Layer over a Rectangular Cavity," *accepted for publication in Journal of Fluid Mechanics*, 2016.
[15] Casper, K. M., Wagner, J. L., Beresh, S. J., Henfling, J. F., Spillers, R. W., & Pruett, B. O., "Complex Geometry Effects on Cavity Resonance," *AIAA Journal*, Vol. 54, No. 1, 2015, pp. 320-330.
[16] Ukeiley, L., Sheehan, M., Coiffet, F., Alvi, F., Arunajatesan, S., and Jansen, B., "Control of pressure loads in geometrically complex cavities," *Journal of Aircraft*, Vol. 45, No. 3, 2008, pp.1014-1024.
[17] DeMauro, E. P., Beresh, S. J., Wagner, J. L., Henfling, J. F., and Spillers, R. W., "Three-Dimensional Measurement of Edge Effects in Open Cavities of Finite-Span," AIAA Paper 2016-3314.
[18] Krishnamurty K., "Acoustic radiation from two-dimensional rectangular cutouts in aerodynamic surfaces," NACA TN 3487, 1955.
[19] Sarohia, V., "Experimental investigation of oscillations in flows over shallow cavities," *AIAA Journal*, Vol. 15, No. 7, 1977, pp. 984-990.
[20] Kegerise, M. A., "An Experimental Investigation of Flow Induced Cavity Oscillations," Ph.D. Thesis, Department of Mechanical Engineering, Syracuse University, New York, USA, 1999.
[21] Kegerise, M. A., Spina, E. F., Garg, S., Cattafesta, L. N., "Mode-Switching and Nonlinear Effects in Compressible Flow Over a Cavity," *Physics of Fluids*, Vol. 16, No. 3, 2005, pp. 678-687.
[22] Larchevêque, L., Sagaut, P., Lê, T. P., and Compte, P., "Large-eddy simulation of a compressible flow in a three-dimensional open cavity at high Reynolds number," *Journal of Fluid Mechanics*, Vol. 516, 2004, pp. 265-301.
[23] Brès, G. A., and Colonius, T., "Three-Dimensional Instabilities in Compressible Flow over Open Cavities," *Journal of Fluid Mechanics*, Vol. 599, 2008, pp. 309-339.
[24] Delprat, N., "Rossiter's formula: A simple spectral model for a complex amplitude modulation process?," *Physics of Fluids*, Vol. 18, No. 7, 2006.
[25] Basley, J., Pastur, L. R., Lusseyran, F., Faure, T. M., & Delprat, N, Experimental investigation of global structures in an incompressible cavity flow using time-resolved PIV," *Experiments in Fluids*, Vol. 50, No. 4, 2011, pp. 905-918.
[26] Hassan, M., Keirsbulck, L., Labraga, L., "Aero-Acoustic Coupling Inside Large Deep Cavities at Low Subsonic Speeds," *Journal of Fluids Engineering*, Vol. 31, No. 1, 2009, pp. 011204
[27] Guéniat, F., Pastur, L., Lusseyran, F., "Investigating mode competition and three-dimensional features from two-dimensional velocity fields in an open cavity flow by modal decompositions," *Physics of Fluids*, Vol. 26, No. 8, 2014 ,pp. 085101
[28] Liu, X., and Katz, J., "Vortex-corner interactions in a cavity shear layer elucidated by time-resolved measurements of the pressure field,".*Journal of Fluid Mechanics*, Vol. 728, 2013, pp. 417-457.
[29] Murray, N. E., and Ukeiley, L. S., "Modified quadratic stochastic estimation of resonating subsonic cavity flow," *Journal of Turbulence*, Vol. 8, No. 53, 2007, pp. 1-22.
[30] Murray, N., Raspet, R., and Ukeiley, L., "Contributions of turbulence to subsonic cavity flow wall pressures," *Physics of* Fluids, Vol. 23, No. 1, 2011, pp. 015104.
[31] Wagner, J. L., Casper, K. M., Beresh, S. J., Arunajatesan, S., Henfling, J. F., Spillers R. W., Pruett, B. O., "Relationship between Acoustic Tones and Flow Structure in Transonic Cavity Flow," AIAA Paper 2015-2937.
[32] Beresh, S. J., Kearney, S. P., Wagner, J. L., Guildenbecher, D. R., Henfling, J. F., Spillers, R. W., Pruett, B. O., Jiang, N., Slipchenko, M., Mance, J., and Roy, S., "Pulse-Burst PIV in a High-Speed Wind Tunnel," *Measurement Science and Technology*, Vol. 26, No. 9, 2015.
[33] Flaherty, W., Reedy, M. T., Elliot, G. S., Austin, J. M., Schmit, Crafton, J., "Investigation of Cavity Flow Using Fast-Response Pressure Sensitive Paint," AIAA Paper 2013-0678.
[34] Casper, K. M., Wagner, J. L., Beresh, S. J., Henfling, J. F., Spillers, R.W., "Unsteady Pressure Sensitive Paint Measurements of Resonance Properties in Complex Cavities," AIAA Paper 2016-3315.

[35] Song, Q., Closed-Loop Control of Flow-Induced Cavity Oscillations, Ph.D. Thesis, Department of Mechanical and Aerospace Engineering, University of Florida, Gainesville, USA, 2008.
[36] Murray, N. E., Sallstrom, E., and Ukeiley, L., "Properties of Subsonic Open Cavity Flow Fields," *Physics of Fluids*, Vol. 21, No. 9, 2009.
[37] Wagner, J. L., Casper, K. M., Beresh, S. J., Pruett, B. O., Spillers R. W., and Henfling, J. F., "Mitigation of Wind Tunnel Wall Interactions in Subsonic Cavity Flows," *Experiments in Fluids*, Vol. 56, 2015.
[38] Samimy, M., and Lele, S. K., "Motion of Particles with Inertia in a Compressible Free Shear Layer," *Physics of Fluids A*, Vol. 3, No. 8, 1991, pp. 1915-1923.
[39] Slipchenko, M. N., Miller, J. D., Roy, S., Gord, J. R., Danczyk, S. A., and Meyer, T. R., "Quasi-Continuous Burst-Mode Laser for High-Speed Planar Imaging," *Optics Letters*, Vol. 37, No. 8, pp. 1346-1348, 2012.
[40] Slipchenko, M. N., Miller, J. D., Roy, S., Gord, J. R., and Meyer, T. R., "All-Diode-Pumped Quasi-Continuous Burst-Mode Laser for Extended High-Speed Planar Imaging," *Optics Express*, Vol. 21, No. 1, pp. 681-689, 2013.
[41] Shaikh, F. N. and Gaster, M., "The Non-Linear Evolution of Modulated Waves in a Boundary Layer*," Journal of Engineering Mathematics*, Vol. 28, 1994, pp. 55–71.
[42] Jordan, D., Miksad, R. W., and Powers, E. J., "Implementation of the Continuous Wavelet Transform for Digital Time Series Analysis," Review of Scientific Instruments, Vol. 68, No. 3, March 1997, pp. 1484–1494.
[43] Torrence, C. and Compo, G. P., "A Practical Guide to Wavelet Analysis," *Bulletin of the American Meteorological Society*, Vol. 79, No. 1, 1998, pp. 61–78.
[44] Russell, D., "Electronic Supplement to Development of a Time-Domain, Variable-Period Surface Wave Magnitude Procedure for Application at Regional and Teleseismic Distances, Part I: Theory," *Bulletin of the Seismological Society of America*, 2006, URL: http://www.seismosoc.org/publications/BSSA_html/bssa_96-2/05055-esupp/.
[45] Heller, H. H., and Bliss, D. B., "The Physical Mechanism of Flow Induced Pressure Fluctuations in Cavities and Concepts for Suppression," AIAA Paper 75-491.
[46] Hussain, A. K. M., "Coherent Structures and Turbulence," *Journal of Fluid Mechanics*, vol. 173, pp. 303-356, 1986.
[47] de Vicente, J., Basley, J., Meseguer-Garrido, F., Soria, J., and Theofilis, V., "Three-dimensional instabilities over a rectangular open cavity: from linear stability analysis to experimentation," *Journal of Fluid Mechanics*, Vol. 748, pp. 189-220.
[48] Seena, A., Sung, H. J., "Spatiotemporal representation of the dynamic modes in turbulent cavity flows," *International Journal of Heat and Fluid Flow*, Vol. 4, 2013, pp. 1-13.
[49] Lee, S. B., Seena, A., Sung, H. J., "Self-sustained oscillations of turbulent flow in an open cavity," *Journal of Aircraft*, Vol. 47, No. 3, 2010, pp. 820-834.
[50] Li, W., Nonomura, T.,Fujii, K., "On the feedback mechanism in supersonic cavity flows," *Physics of Fluids*, Vol. 25, No. 5, 2013, pp. 056101.
[51] Lee, B. H. K., "Effect of Captive Stores on Internal Weapons Bay Floor Pressure Distributions, *Journal of Aircraft*, Vol. 47, No. 2., 2010, pp. 732-735.
[52] Roberts, D. A., Stokes, N. P., Quinn, M. K., Coppin, J., and Birch, T. J., "Evaluation of Dynamic Pressure-Sensitive Paint for Improved Analysis of Cavity Flows and CFD Validation," AIAA Paper 2016-0311.
[53] Rockwell, D., and Knisely, C., "The organized nature of flow impingement upon a corner," *Journal of Fluid Mechanics*, Vol. 93, No. 3, 1979 pp. 413-432.
[54] Knisely, C., and Rockwell, D., "Self-sustained low-frequency components in an impinging shear layer," *Journal of Fluid Mechanics*, Vol. 116, 1982, pp. 157-186.
[55] Najm, H. N., and Ghoniem, A. F., "Numerical Simulation of the Convective Instability in a Dump Combustor," *AIAA Journal*, Vol. 29, No. 6, 1991, pp. 911-919.
[56] Lin, J. C., and Rockwell, D., "Organized Oscillations of Initially Turbulent Flow Past a Cavity," *AIAA Journal*, Vol. 39, No. 6, 2001, pp. 1139-1151.
[57] Beresh, S. J., Wagner, J. L., DeMauro, E. P., Henfling, J. F., and Spillers, R. W, "Resonance Characteristics of Transonic Flow over a Rectangular Cavity using Pulse-Burst PIV", AIAA Paper 2016-2044, also to be submitted to *Physical Review Fluids*.
[58] Zhuang, N., Alvi, F. S., Alkislar, M. B., and Shih, C., "Supersonic Cavity Flows and Their Control," *AIAA Journal*, Vol. 44, No. 9, 2006, pp. 2118-2128.
[59] Bian, S., Driscoll, J. F., Elbing, B. R., and Ceccio, S. L., "Time Resolved Flow-Field Measurements of a Turbulent Mixing Layer over a Rectangular Cavity," *Experiments in Fluids*, Vol. 51, No. 1, 2011, pp. 51-63.
[60] Haigermoser, C., Vesely, L., Novara, M., and Onorato, M., "A Time-Resolved Particle Image Velocimetry Investigation of a Cavity Flow with a Thick Incoming Turbulent Boundary Layer, *Physics of Fluids*, Vol. 20, No. 10, 2008, pp. 105101.

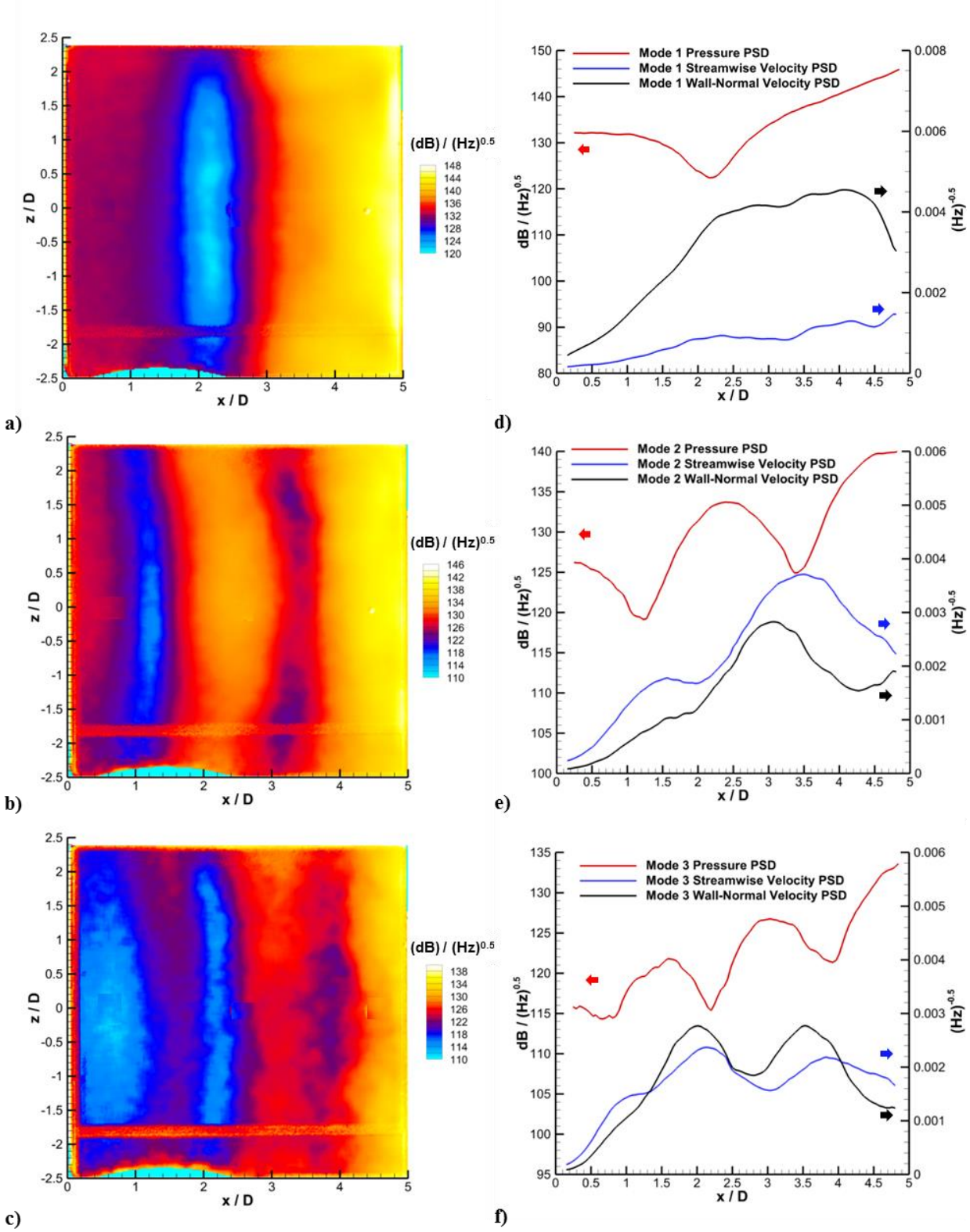

Fig. 12 Spatial distributions of cavity floor pressure PSD amplitudes corresponding to cavity modes (a) one, (b) two, and (c) three. Streamwise profiles of centerline pressure PSD amplitude and averaged velocity PSD amplitude corresponding to modes (d) one, (e) two, and (f) three.

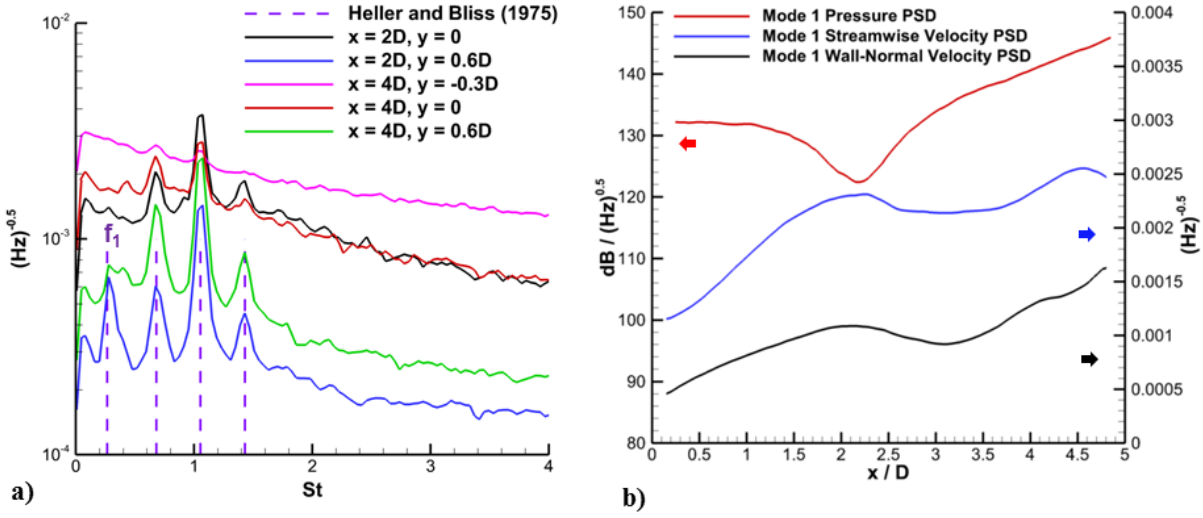

Fig. 13 Mode one acoustics: (a) PSD spectra at five points within the cavity using all 245 time-sequences, and (b) streamwise profiles of mode one velocity PSD amplitude averaged over the upper half of the measurement domain.

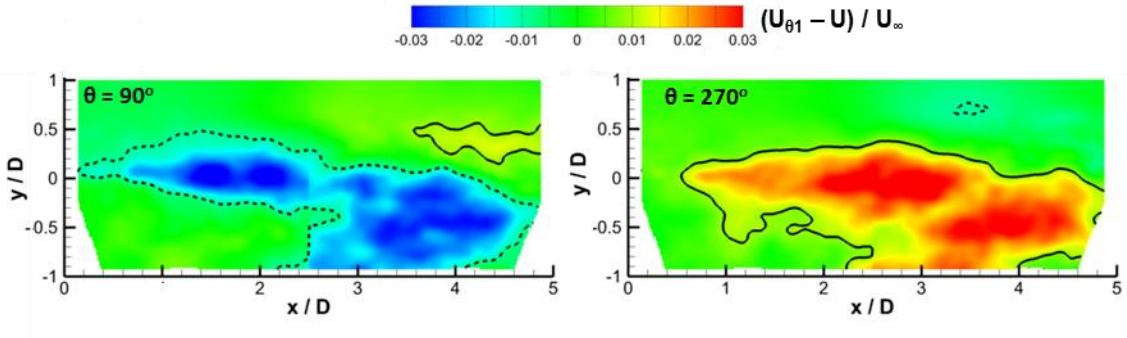

Fig. 14 Mode one coherent flow structures ($U_\theta - U$) obtained with phase averaging of 10-Hz PIV data. Solid and dashed lines correspond to 0.017U_∞ and -0.017U_∞, respectively.

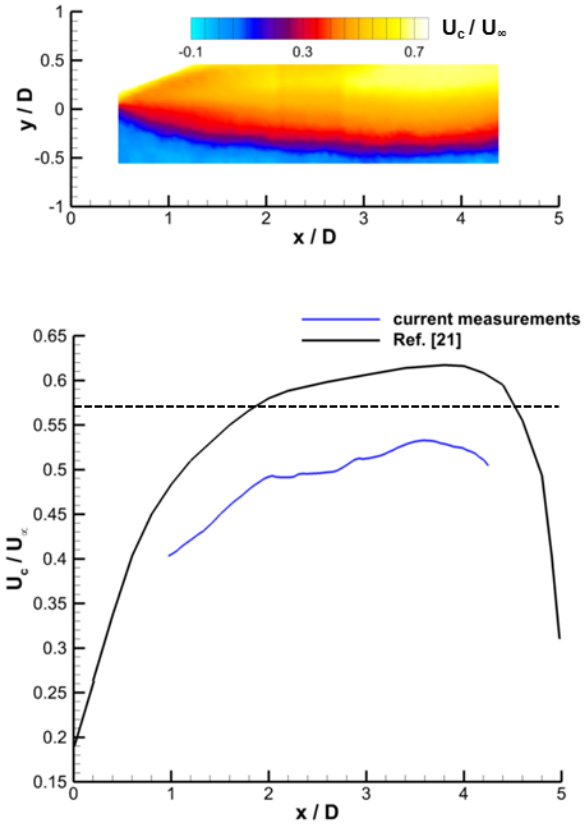

Fig. 15 Unfiltered convective velocities based on the wall-normal component of raw velocity: (a) distribution within the cavity, and (b) centerline profile compared to the simulations of Larchevêque et al. [21]. Dashed line corresponds to $U_c = 0.57U_\infty$.

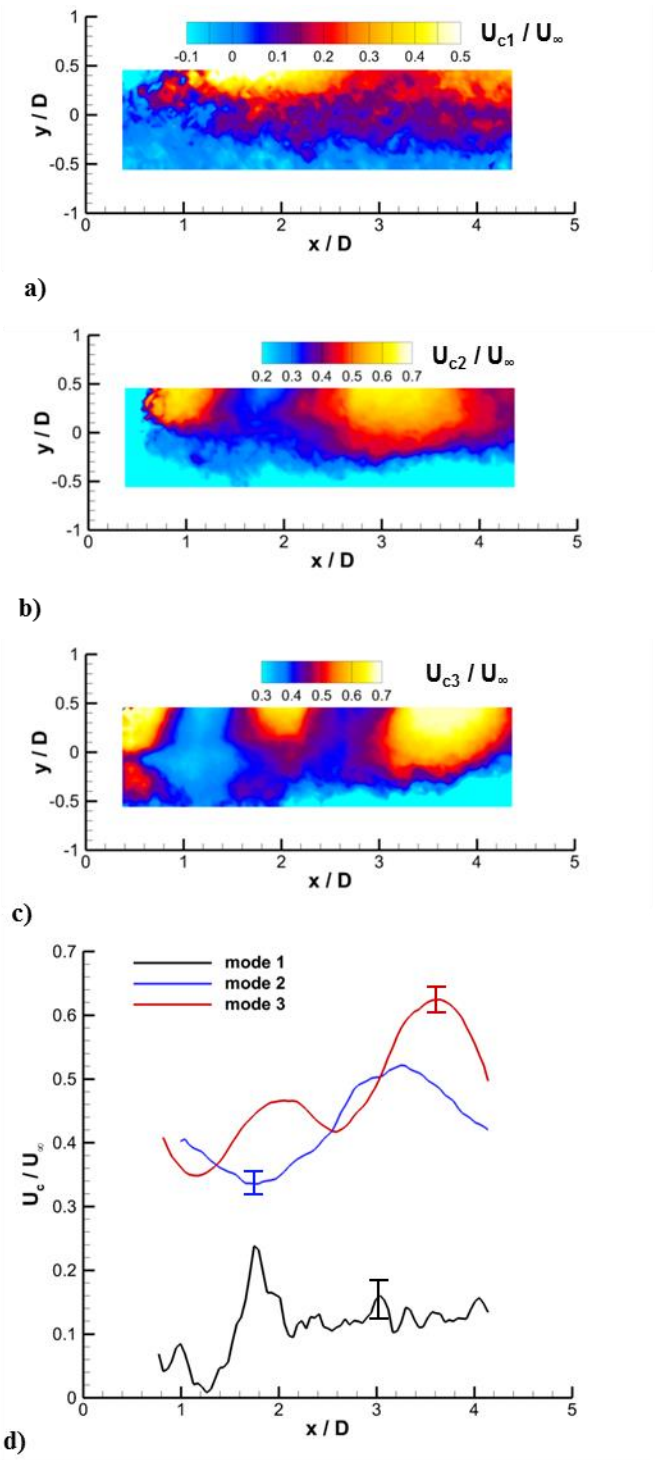

Fig. 16 Modal convective velocities based on the wall-normal component of filtered velocity: a) mode 1, b) mode 2, c) mode 3 and d) streamwise profiles at y = 0. Error bars represent the precision uncertainty with 95% confidence intervals.

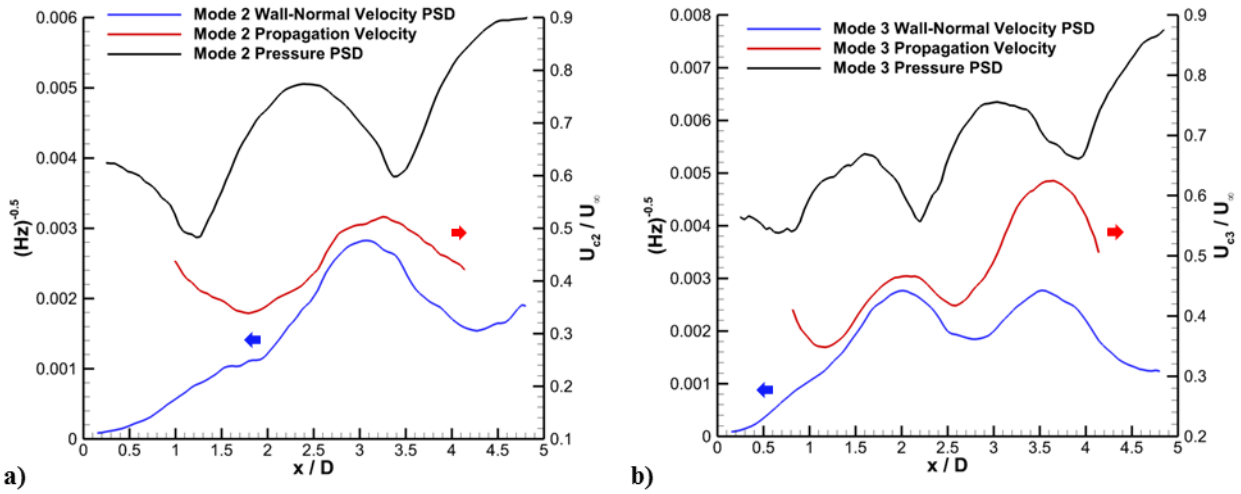

Fig. 17 Streamwise distributions of modal propagation velocity at y = 0, wall-normal velocity PSDs averaged over the measurement height, and centerline pressure PSD amplitudes at: (a) Mode 2, and (b) Mode 3. The pressure distributions are on the same scale as in Fig. 16, which is not shown here for figure clarity.